A New Class of Lithium Hybrid Gel Electrolyte Systems

V. Di Noto,*,† M. Vittadello,† S. G. Greenbaum,‡ S. Suarez,‡ K. Kano,§ and T. Furukawa§

Dipartimento di Scienze Chimiche, Università di Padova, Via Marzolo 1, I-35131 Padova, Italy, Physics Department, Hunter College of CUNY, 695 Park Avenue, New York, New York 10021, and Department of Chemistry, Faculty of Science, Tokyo University of Science, 1-3 Kakurazaka, Shinjuku-ku, Tokyo 162-8601, Japan

Received: June 15, 2004; In Final Form: September 17, 2004

This report describes new materials prepared by using Li_2PdCl_4 [or $(CH_3)_2SnCl_2$], $Li_3Fe(CN)_6$ and glycerol, as precursors. The nearly instantaneous sol ⇒ gel process followed by complete dehydration under reduced pressure produced the $[Fe_xPd_y(CN)_zCl_v(C_3H_8O_3)Li_l]$ (**I**) and $[Fe_xSn_y(CH_3)_{2y}(CN)_zCl_v(C_3H_8O_3)Li_l]$ (**II**) materials with the characteristics of a hybrid inorganic−organic gel (HGE), as confirmed by morphological studies. FIR, MIR, Raman laser, and UV−visible investigations together with detailed compositional data allowed us to propose a structural hypothesis and to describe the interactions between ions and glycerol in these materials. We concluded that the two HGEs consist of a hybrid backbone composed of a mixture of inorganic−organic clusters of Fe and Pd (or Sn) structural units with glycerol surrounded by nonbonded glycerol molecules. The materials **I** and **II** are thermally stable up to ∼115 and ∼125 °C, respectively. DSC investigations revealed their T_g at −74 and −76 °C, respectively. Variable-temperature ^1H and ^7Li NMR line width, spin−lattice relaxation, and pulsed field gradient diffusion measurements were performed to investigate a possible correlation between glycerol mobility and lithium migration. Electrical spectroscopy measurements in the 10 mHz to 1 GHz range taken from −60 to +80 °C provided information regarding the systems' conductivity mechanism and structural relaxations. In addition, electrical spectra in the high-frequency region revealed the presence of an α relaxation event associated with glycerol molecules. This phenomenon suggests that the proposed HGEs exhibit the glycerol glass-forming behavior typical of supercooled materials. Finally, HGEs **I** and **II** exhibited room temperature conductivities of 5.0×10^{-5} S·cm^{-1} and 8.5×10^{-5} S·cm^{-1}, respectively, which classify these materials as good ion conductors.

1. Introduction

The applicability of lithium-polymer technology is currently feasible due to research efforts undertaken in the field of polymer gel electrolytes.[1,2] The previously proposed Zeolitic Inorganic−Organic Polymer Electrolytes (Z-IOPE)[3] exhibit a plastic consistency. Z-IOPEs consist of an inorganic−organic network whose cavities are flooded with a liquid polymer electrolyte formed in situ.[3−7] These systems share the following essential characteristics: (a) suitable organic macromolecules are linked to one another by bridging inorganic clusters; (b) inorganic clusters are formed by the aggregation of two or more inorganic coordination complexes; and (c) inorganic clusters can be either positively or negatively charged. These systems are generally prepared by a sol ⇒ gel ⇒ plastic transition and show high ionic conductivities (up to 10^{-5} S·cm^{-1} at room temperature). The first two representative examples of Z-IOPEs were obtained from K_2PdCl_4, $K_3[Fe(CN)_6]$, and poly(ethylene-glycol)600 (PEG600)[3] and from K_2PdCl_4, $K_3[Co(CN)_6]$, and PEG 600.[4] Other examples of Z-IOPE networks were synthesized from $SnCl_4$, $K_4[Fe(CN)_6]$, and PEG600[5] or from $(CH_3)_2SnCl_2$, $K_4[Fe(CN)_6]$, and PEG600.[6,7] Lithium Z-IOPEs based on Li_2PdCl_4, $Li_3[Fe(CN)_6]$, and PEG600[8] and on $(CH_3)_2SnCl_2$, $Li_3[Fe(CN)_6]$, and PEG600[9] have also been described. The Z-IOPE materials are noncrystalline and therefore can be classified (together with other polymer-based systems, glassy ceramics, and amorphous metals) into the wide realm of glasses, in accordance with the most recent developments in this field.[1]

The analogy of Z-IOPEs with gel electrolytes suggests the possibility of employing a combination of hard and soft metal precursors in a sol ⇒ gel process to give rise to hybrid gels with use of lower molecular weight organic ligands such as glycerol instead of PEG600. Glycerol is a very well-known glass former[10] that has been thoroughly investigated in broadband dielectric spectroscopy[11] and thermodynamic studies.[12,13] On the basis of the "strong-fragile" classification scheme introduced by Angell,[10,12,13] glycerol is considered to be a strong glass former and therefore is characterized by a molecular relaxation (namely, the α-relaxation time τ_α) that increases with an almost VTF-like (simple activated) profile.[11] The analysis of glycerol's frequency-dependent dielectric loss $\epsilon''(\nu)$ reveals that it is a "Type A" glass former,[10,14] since it exhibits well-defined α-relaxation followed by an excess wing, without any slow β-relaxation[14] (as in the case of "type B" glass formers). Therefore, glycerol appears as a suitable organic molecule for investigating the effect of inorganic clusters in an electrolytic gel structure. Glycerol also represents a promising precursor for the preparation of gel lithium ion conductors able to operate at low temperatures owing to the absence of thermal transitions over a wide temperature range.[10,14]

The analogy between electrolytic polymer complexes and glasses has already proven to be fruitful. Indeed, superionic

* To whom correspondence should be addressed. E-mail: vito.dinoto@unipd.it.
† Università di Padova.
‡ Hunter College of CUNY.
§ Tokyo University of Science.

10.1021/jp047413x CCC: $27.50 © 2004 American Chemical Society
Published on Web 11/11/2004

glasses such as LISICONS[1] provided the motivation for the development of "polymer-in-salt" materials,[15] in which low-temperature melts of appropriate alkali−cation−salt mixtures are blended with small quantities of various polymers. This salt−polymer mixture represents a rubbery version of a glassy electrolyte, with a significant increase in lithium ion mobility. The cationic transport number t_+ is equal to 1, as in superionic glass electrolytes. However, high concentrations of the salt unfortunately give rise to an undesirable increase in the glass transition temperature T_g, resulting in conductivities lower than 10^{-4} S·cm^{-1} at room temperature.

The present study investigated a new class of hybrid inorganic−organic gels (Hybrid Gel Electrolytes or HGEs) based on either Li_2PdCl_4 or $(CH_3)_2SnCl_2$ plus $Li_3Fe(CN)_6$ and glycerol, which were synthesized through a sol ⇒ gel transition. The structures of the resulting materials were examined by vibrational (mid-infrared, far-infrared and Raman) and UV−visible spectroscopy. The materials were also subjected to morphological investigations by scanning electron microscopy and thermal analyses, using thermogravimetry (TG) and differential scanning calorimetry (DSC). Ion transport dynamics in the HGE systems were analyzed by means of ^{1}H and ^{7}Li solid-state NMR spectroscopy and broad-band dielectric measurements in the 10 mHz to 1 GHz frequency range.

2. Experimental Section

2.1. Reagents. $(CH_3)_2SnCl_2$ and glycerol (Aldrich, ACS grade) were used as received. Li_2PdCl_4 was prepared by reacting $PdCl_2$ (Carlo Erba, ACS grade) and LiCl (Carlo Erba, ACS grade), as in ref 8. The $Li_3Fe(CN)_6$ salt was synthesized through the intermediate $Ag_3Fe(CN)_6$ (Aldrich, ACS grade) from $K_3Fe(CN)_6$ (Aldrich, ACS grade) and LiCl (Carlo Erba, ACS grade), as in ref 8. All transfer and handling operations of final products were performed in an argon atmosphere.

2.2. Instruments and Methods. Microanalysis to determine Li, Fe, Pd, and Sn content in the gel electrolytes was performed by inductively coupled plasma atomic emission spectrometry (ICP-AES), using the method of standard additions and a spectroflame Modula sequential and simultaneous ICP-AES spectrometer equipped with a capillary cross-flow nebulizer (Spectro Analytical, Kleve, Germany). The following emission lines were used: λ(Li) = 670.784 nm; λ(Fe) = 259.940 nm; λ(Pd) = 340.458 nm; λ(Sn) = 189.926 nm; argon reference line = 430.01 nm. A plasma power of 1.2 kW, a radio frequency of 27.12 MHz, and an argon gas flow with nebulizer, auxiliary, and coolant controls set at 1, 0.5, and 14 L/min, respectively, were used. Measurements were performed on samples that had been microwave-digested by using a CEM MDS-2100 microwave system. Gel electrolyte mineralization was performed by treating 100.0 mg of each sample with a solution consisting of HNO_3 (70%) 54% vol, HCl (37%) 31% vol, and H_2O 15% vol.

The morphology was investigated by using a Cambridge Stereoscan 250 Mark 1 scanning electron microscope (SEM), with an acceleration voltage of 25 kV. The sample was graphite-coated with a Balzer mod. Med. 010(6) sputtering unit operating at 0.2 mbar. Elemental X-ray fluorescent microanalyses were performed with a SEM EDAX PW9800 system coupled with an energy-dispersive X-ray spectrometer and equipped with a Si/Li detector.

Thermogravimetric analyses were carried out with an SDT 2960 thermobalance interfaced with a Nicolet Medium FT-IR Nexus to monitor exhaust gases. The TG profile was recorded under an N_2 flux of 70 cm^3/min and a heating rate of 10 deg/min. The measurements were performed on ca. 18 mg of sample in an open platinum pan.

DSC measurements were carried out with use of a DSC 2920 differential scanning calorimeter (TA Instruments) equipped with the LNCA low-temperature attachment operating under N_2 flux of 70 cm^3/min. Measurements were made over a temperature range of −150 to +200 °C and a heating rate of 10 deg/min on ca. 10 mg of sample that had been sealed under nitrogen in an aluminum pan. The T_g (glass transition temperature) was determined at the middle of the heat capacity change of the glass transition process.

FT-IR spectra in the medium (MIR)- and far (FIR)-infrared regions were obtained by using Nicolet FT-IR Nexus and Nicolet 5SxC spectrometers, respectively. Both were equipped with a triglycine sulfate (TGS) detector at a resolution of 4 cm^{-1}. The Happ−Genzel apodization method was employed. MIR measurements were derived by averaging 1000 scans obtained on samples dispersed in anhydrous KBr pellets and sealed in an argon cell with KBr windows. Far-IR spectra were derived by averaging 2000 scans obtained on samples spread as thin films between two polyethylene windows in a cell hermetically sealed under argon. The MIR spectrum was decomposed with Gaussian functions, using a homemade computer program as reported elsewhere.[3,5] The baseline correction was performed with the Nicolet FT-IR Nexus spectrometer software.

Raman spectra were measured with polarized light, using a $\lambda/4$ polarizer with a Czerny-Turner double monochromator at a focal distance of 400 mm and a grating of 1800 lines/mm blazed at 5000 Å. The light source was a Spectra-Physics Stabilite 2016 Argon Ion Laser, and the excitation line was set at 514.5 nm. A JASCO type HTV-R374 photomultiplier tube was used to collect scattered light. The spectra were acquired at 90 °C and with a spectral slit width of 4 cm^{-1}, an integrating time of 3 s, and an increment of 1.0 cm^{-1}. The spectra were recorded at room temperature on samples sealed under argon in quartz tubes forced to axial rotation; the results represent the average of three spectra.

UV−visible spectra were collected with a Spectronic Unicam UV 500 UV−visible spectrometer. Deuterium and tungsten lamps were employed for the 190−340- and 340−900-nm ranges, respectively; samples were sealed under nitrogen in a stainless steel cell equipped with quartz windows.

^{1}H and ^{7}Li NMR information was obtained on a Chemagnetics spectrometer in conjunction with a 7.1 T Japan Technology superconducting magnet; the ^{1}H and ^{7}Li Larmor frequencies were 301 and 116 MHz, respectively. Spectral information was derived by Fourier transforming the FID's of single pulse sequences obtained with use of $\pi/2$ pulse widths of 12 and 5 μs for ^{1}H and ^{7}Li, respectively. Spin−lattice relaxation times (T_1) were measured by using the inversion recovery pulse sequence ($\pi - \tau - \pi/2$) with approximately 15 τ values. Self-diffusion coefficients (D) were obtained by the Pulse Gradient Spin−Echo technique,[9] with gradient (δ) on and gradient delay (Δ) times of 8−10 and 10−18, and 9 and 15 ms respectively for ^{1}H and ^{7}Li. The temperature range investigated was 300−370 K, with 20−25 min allowed for equilibration between temperature changes.

Experimental complex permittivity spectra in the 10 mHz to 1 GHz frequency range were obtained by using[16] a laboratory-made dielectric spectrometer consisting of a charge amplifier and a digital data acquisition system (10 mHz to 100 kHz range), a Hewlett-Packard HP4192ALF (5 Hz to 13 MHz range), and a HP4191ARF (1 MHz to 1 GHz range). Samples were sandwiched in 20 mm diameter circular stainless steel electrodes, using a 125 μm diameter fused silica fiber spacer. The samples were placed in a temperature-controlled cryostat (Torisha Co.),

TABLE 1: Microanalytical Data and Molar Ratios for Complexes I and II

compd		microanalytical[a] data (%)	molar ratios[b]	
I	C	37.30 (3.1057)	n_{Pd}/n_{gly}	0.0120
	N	0.68 (0.0485)	n_{Fe}/n_{gly}	0.0081
	H	9.15 (9.0774)	n_{Li}/n_{gly}	0.0509
	Fe	0.46 (0.0082)	n_{CN}/n_{gly}	0.0476
	Pd	1.30 (0.0122)		
	Li	0.36 (0.0519)		
II	C	39.11 (3.2564)	n_{Sn}/n_{gly}	0.0176
	N	0.59 (0.0421)	n_{Fe}/n_{gly}	0.0072
	H	9.00 (8.9286)	n_{Li}/n_{gly}	0.0189
	Fe	0.40 (0.0072)	n_{CN}/n_{gly}	0.0490
	Sn	2.07 (0.0174)		
	Li	0.13 (0.01873)		

[a] Fe, Pd, Sn and Li were determined by ICP-AES spectroscopy. Molar values in parentheses. [b] n_{gly} are the moles of glycerol.

with an N_2 gas jet heating and cooling system working from −170 to +200 °C. The equation $\sigma^* = i\omega\epsilon^*$ ($\sigma' = \omega\epsilon''$, $\sigma'' = \omega\epsilon'$) was used to convert the complex permittivity ($\epsilon^* = \epsilon' - i\epsilon''$) into complex conductivity ($\sigma^* = \sigma' + i\sigma''$), where $\omega = 2\pi f$ (f in hertz). σ^* spectra were employed to investigate the AC electric response of the HGE samples and to detect the corresponding bulk dc conductivity σ_{dc}. The electrolyte−electrode contact surface and distance between electrodes were micrometrically determined to obtain the cell constants. The temperature was measured with an accuracy greater than ±0.1 °C. Calculated conductivity values showed less than 2% error.

2.3. Synthesis of the HGE Systems. The synthesis of the new HGE electrolytic complexes required the combination of two solutions (A and B). The $[Fe_xPd_y(CN)_zCl_v(C_3H_8O_3)Li_l]$ (**I**) system was prepared by mixing solutions A and B under argon atmosphere. Solution A (red in color) contained 1.1822 g of Li_2PdCl_4 ($4.511 \cdot 10^{-3}$ mol) dissolved in 10.0 g of glycerol. Solution B (bright yellow) contained 0.5126 g of $Li_3Fe(CN)_6$ (2.202×10^{-3} mol) dissolved in 12.5 g of glycerol.

Solutions A and B were mixed in a 250-mL sealed vessel, which rapidly yielded dark-brown gel. After 1 week, release of a small amount of glycerol was noted. The material was filtered on paper under argon atmosphere and left under a vacuum for 2 days at 10^{-2} mbar, and for 1 week at 10^{-5} mbar. The final product was paste-like and dark-brown with a greenish cast. The $[Fe_xSn_y(CH_3)_{2y}(CN)_zCl_v(C_3H_8O_3)Li_l]$ (**II**) system was synthesized by mixing A and B solutions in open air. Solution A (pale pink) contained 1.0499 g of $(CH_3)_2SnCl_2$ (4.780×10^{-3} mol) dissolved in 10.0 g of glycerol, and solution B (bright yellow) contained 0.5075 g of $Li_3Fe(CN)_6$ (2.180×10^{-3} mol) dissolved in 12.5 g of glycerol. Stirring of A with B immediately yielded a yellow-orange gel. The material was filtered on paper and left under a vacuum for 2 days at 10^{-2} mbar and for 1 week at 10^{-5} mbar. These incubations yielded a yellow-orange gel with a slightly green cast. Analytical data and molar ratios for the two synthesized electrolytic complexes are reported in Table 1.

3. Results and Discussion

3.1. Observations and Mechanistic Hypotheses for the Sol−Gel Polycondensation Reaction. The protocol adopted to prepare HGEs systems **I** and **II** is summarized in Scheme 1. As described in the Experimental Section, two solutions were prepared separately and subsequently mixed together. Solutions A and B, used to make system **I**, contained Li_2PdCl_4 and glycerol (A) and $Li_3Fe(CN)_6$ and glycerol (B). Solutions A and B, used to make system **II**, contained $(CH_3)_2SnCl_2$ and glycerol (A) and $Li_3Fe(CN)_6$ and glycerol (B).

SCHEME 1: Synthesis of Hybrid Inorganic−Organic Gel Polymer Electrolytes Based on Li_2PdCl_4 (I) or $Sn(CH_3)_2Cl_2$ (II) Plus Glycerol and $Li_3Fe(CN)_6$

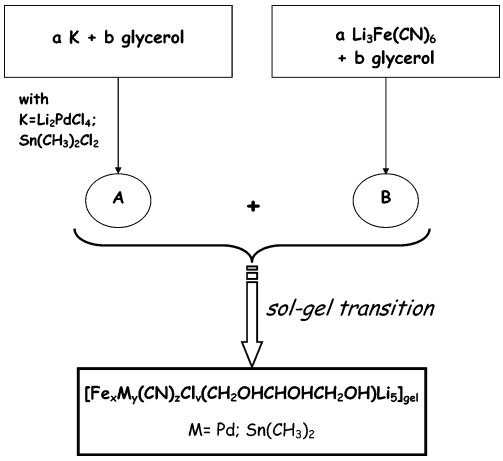

In accordance with previous findings, we are convinced that the sol → gel transition for both HGEs occurs owing to well-established reactions:[3−8] the Cl^- ligand, which is a good leaving ion, in both $PdCl_4^{2-}$ and $(CH_3)_2SnCl_2$, may be substituted by either the nitrogen atom of $Fe(CN)_6^{3-}$ cyanometalate or the hydroxyl group of glycerol. As previously demonstrated, the sol−gel reaction involves the direct substitution of Cl^- leaving groups in $PdCl_4^{2-}$ and $(CH_3)_2SnCl_2$ by oxygen

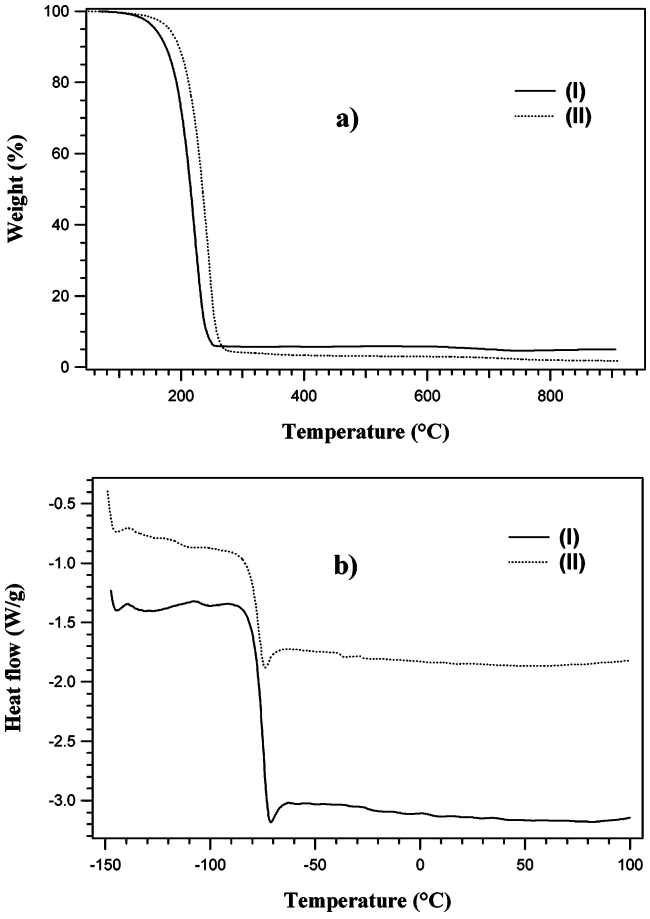

Figure 1. Thermal analyses of $[Fe_xPd_y(CN)_zCl_v(C_3H_8O_3)Li_e]$ (**I**) and $Fe_xSn_y(CH_3)_{2y}(CN)_zCl_v(C_3H_8O_3)Li_e]$ (**II**) HGEs: (a) TG profiles and (b) DSC curves.

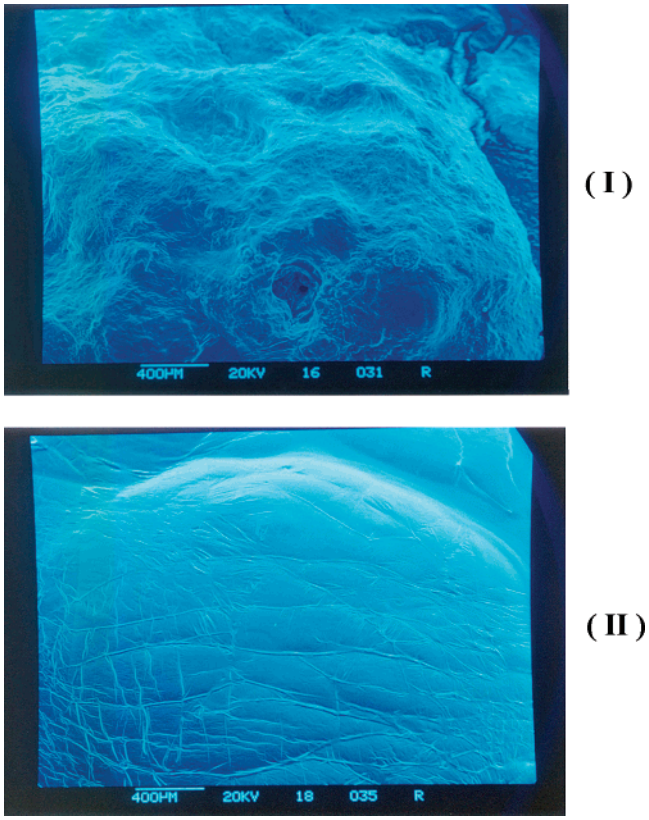

Figure 2. SEM micrographs of $[Fe_xPd_y(CN)_zCl_v(C_3H_8O_3)Li_e]$ (**I**) and $Fe_xSn_y(CH_3)_{2y}(CN)_zCl_v(C_3H_8O_3)Li_e]$ (**II**) HGEs.

ligands. These processes generate a mixture of Pd or Sn hydroxyl complexes, which upon addition of solutions A and B triggers the concatenation of metal complexes through polycondensation reactions, thus increasing the number of intermetallic bridging bonds responsible for formation of the gel network.

Catenation is a well-known process in organo-tin chemistry. Indeed, $(CH_3)_2SnCl_2$ readily forms bridging anionic groups that raise the coordination number of Sn to 6 in an octahedral geometry with *trans*-methyl groups.[17,18] Table 1 reports the analytical data and n_{Pd}/n_{gly}, n_{Sn}/n_{gly}, n_{Fe}/n_{gly}, n_{Li}/n_{gly}, and n_{CN}/n_{gly} molar ratios for the two systems, both of which exhibit the consistency of a solid gel.

3.2. Thermal Analysis and Morphology Investigations. The thermograms shown in Figure 1a indicate that HGEs **I** and **II** are thermally stable up to 115 and 125 °C, respectively. At higher temperatures an intense mass elimination is detected in the 115−225 and 125−240 °C temperature region, respectively. This phenomenon is attributed to the decomposition of the glycerol component. It is noteworthy that the HGE **II**, which is based on Sn complexes, is slightly more stable than HGE **I**, which is based on Pd.

Figure 1b shows the DSC profiles of the two HGEs over their range of thermal stability. Only one event associated with the glass transition (T_g) temperature was detected for HGEs **I** and **II**, at −74 and −76 °C, respectively. The T_g values of **I** and **II** were detected at higher temperatures (i.e., 199 and 197 K) with respect to that of pristine glycerol (185 K). Furthermore, if we consider that glycerol is the major component of HGEs, representing 93.82% and 91.14% of **I** and **II**, respectively, along with the sharp T_g transitions registered in the DSC profiles, we realize that the glycerol units in the HGEs are involved in intermolecular interactions that differ from those usually present in pristine liquid glycerol.

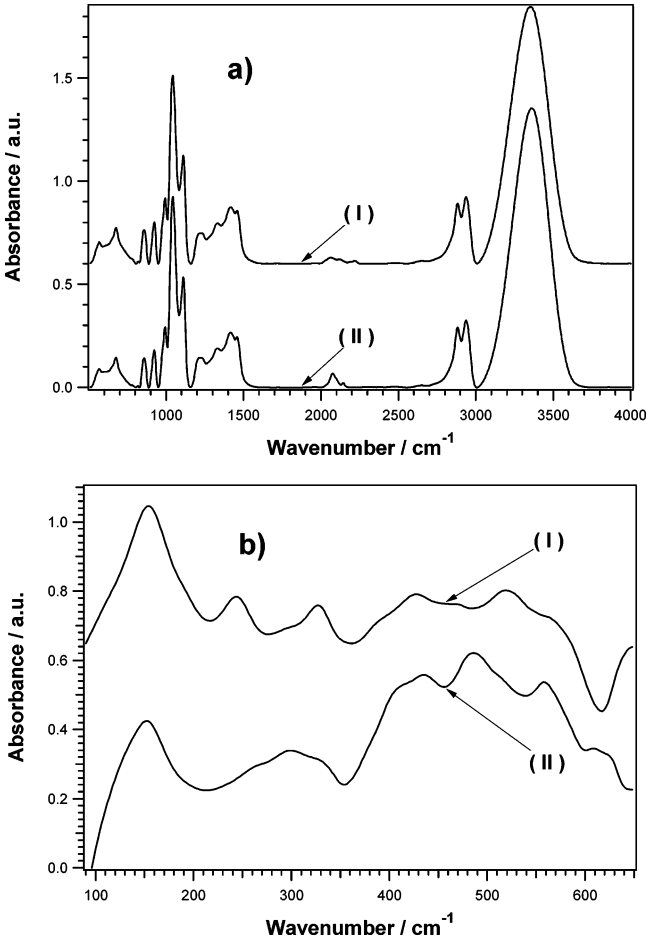

Figure 3. MIR (a) and far-IR (b) FT-IR spectra of $[Fe_xPd_y(CN)_zCl_v(C_3H_8O_3)Li_e]$ (**I**) and $Fe_xSn_y(CH_3)_{2y}(CN)_zCl_v(C_3H_8O_3)Li_e]$ (**II**) HGEs.

The morphology of HGEs **I** and **II** was investigated by SEM measurements. The micrographs reported in Figure 2 show that HGE **I** has the appearance of a compact granular soft paste with empty microcavities. HGE **II** exhibits a different morphology that resembles a smooth gummy paste with wrinkle-like surfaces irregularities. The granularity observed for HGE **I** is completely absent from **II**. The homogeneity of the materials was confirmed by backscattering image measurements and microanalyses carried out on different portions of the samples by X-ray fluorescence with dispersive energy spectroscopy (XRD-EDS). Results indicated that the elements composing **I** and **II** are uniformly distributed in the bulk materials. These SEM results allow us to conclude that the two HGEs are highly homogeneous products whose morphology depends on the chloro−metal complex used as a precursor in the preparation.

3.3. FT-IR, Raman, and UV−Vis Studies. FT-IR, Raman, and UV−vis investigations were carried out in order to arrive at a possible structural hypothesis for the HGE materials and to understand the interactions between the inorganic moieties and glycerol molecules. In particular, UV−vis studies were performed in order to check the oxidation states, and the coordination stereochemistry of transition metal atoms in terms of metal−ligand bonds. FT-IR and Raman studies were carried out in order to detect the conformation of glycerol molecules and the interactions of glycerol−glycerol and glycerol−inorganic components.

The MIR spectra (Figure 3) include absorption bands assigned to glycerol vibrational modes[19,20] and to cyanide groups of cyanometalate complexes[3−8,21,22] (region 2000−2300 cm^{-1} (Figure 3a)). The 3500−3000-cm^{-1} region shows a single very

TABLE 2: FT-IR and Raman Band Assignments of the I and II Complexes

obsd freq (cm^{-1})[a]					
I		**II**			
IR	Raman	IR	Raman	band assignment[b,c]	ref
3354 (vs)	3350 (vw)	3359 (vs)	3350 (vw)	ν(OH)	19, 20
2937 (s)	2937 (s)	2937 (s)	2936 (s)	ν^a(CH)	19
2883 (s)	2887 (s)	2883 (s)	2890 (s)	ν^s(CH)	19
2218 (vw)	2220 (w)				
2185 (vw)	2201 (vw)	2144 (vw)	2187 (vw)	ν(CN_b)	3−8, 21, 22
2158 (vw)		2103 (vw)	2151 (vw)	ν(CN_b)	3−8, 21, 22
2126 (vw)	2127 (vw)	2073 (w)	2093 (vw)	ν(CN_t)	3−8, 21, 22
2063 (vw)					
2025 (vw)		2038 (vw)		ν(CN_t)	3−8, 21, 22
1458 (s)	1460 (s)	1458 (s)	1460 (s)	sr(CH_2)	19, 23
1415 (s)		1415 (s)			
1373 (m,sh)	1379 (vw)	1373 (m,sh)	1377 (vw)	$\delta_{in\ plane}$(OH), w(CH_2)	19, 23
1331 (m)	1329 (vw)	1331 (m)	1328 (vw)		
1282 (w)	1310 (vw)	1282 (w)	1307 (vw)		
1232 (w)	1247 (w)	1230 (m)	1252 (w)	$\delta_{in\ plane}$(OH), w(CH)	19, 23
1215 (w)	1208 (vw)	1213 (vw)	1212 (w)		
1111 (vs)	1107 (m)	1111 (vs)	1109 (m)	ν^{sec}(C−C−O) out of phase	19, 23
1041 (vs)	1050 (vs)	1043 (vs)	1055 (vs)	ν^{pri}(C−C−O) out of phase	19, 23
993 (s)	977 (vw)	993 (s)	979 (vw)	ν(CO), T	19, 23
924 (m)		924 (m)		ν(CO), G	19, 23
858 (m)		858 (m)		ν^{sec}(C−C−C)	19, 23
820 (vw)		818 (vw)		ν^{pri}(C−C−C)	19, 23
675 (m)		675 (m)		δ(C−C−O)	19, 23
654 (w)		652 (w)			
577 (w)				ν(Fe−CN)	3, 6, 8
559 (vw)		557 (w)			
515 (vw)				ν^a(Pd−N)	4
		511 (vw)		ν(Sn−O)	6
494 (vw)				ν^s(Pd−N)	4
		486 (vw)		ν(Sn−C)	6
474 (vw)				ν(Pd−O)	4
444 (vw)		434 (vw)		ν(Li−O)	8
		413 (vw)		ν(Sn−N)	6
399 (vw)				δ(C−Fe−C)	8
386 (vw)				ν^a(Pd−Cl)	8, 4
330 (vw)		330 (vw)		φ_i(CC), δ(CCO) A_g of glycerol mode 11	23, 24
303 (vw)				ν^s(Pd−Cl)	8, 4
		299 (vw)		ν(Sn−Cl)	6
264 (vw)		266 (vw)		φ_i(CC), δ(CCO) A_g of glycerol mode 5	23, 24
215 (vw)				ν(Pd−O)	8, 4
137 (w)		152 (w)		φ_i(CC), δ(CCO) B_2 of glycerol mode 13	23, 24

[a] Relative intensities of observed bands are reported in parentheses: vs, very strong; s, strong; m, medium; w, weak; vw, very weak; sh, shoulder. [b] ν, stretching; δ, bending; w, wagging; sr, scissoring; φ_i, internal rotations; a, antisymmetric mode; s, symmetric. [c] T, trans; G, gauche; pri, primary alcohol; sec, secondary alcohol.

intense band peaking at ca. 3354 cm^{-1}, which is assigned to the hydrogen-bonded ν(OH) vibration. This band is very broad in pristine glycerol and is registered at 3365 cm^{-1} (data not shown). Therefore, the hydrogen bond structure of pristine glycerol shifts the ν(OH) vibration to higher frequencies by about 12 cm^{-1}. By applying the previously proposed[20] empirical rule, it is possible to estimate that the hydrogen bond strength in pure glycerol is higher than that in HGE materials by about 1 kJ mol^{-1} (0.4 kcal mol^{-1}). The complete assignments of the FT-IR spectra shown in Figure 3 are provided in Table 2. The vibrational region from 1415 to 924 cm^{-1} is useful to studying the possible coordination interactions between oxygen atoms of glycerol and the inorganic components. Indeed, the hydroxyl groups of glycerol contribute significantly to the vibrational modes registered in this region and in general are expected to be involved both in the hydrogen bonding structure and in the coordination of the inorganic components of the materials. It is important to note that the spectra shown in Figure 3a coincide quite well with that proposed in the literature for a conformational mixture of glycerol molecules[23,24] consisting predominantly of $\alpha\alpha 1$, $\alpha\gamma$, and $\gamma\gamma$ conformers with fractional concentrations of 0.74, 0.07, and 0.19, respectively.[23] It should be pointed out that in accordance with Bastiansen,[25] each CH_2OH group of glycerol could rotate around a CC covalent bond, thereby giving rise to three conformations termed α, β, and γ. In the α conformation, the end oxygen atoms of the CH_2OH groups are in the trans position. In the β conformation, the two oxygen atoms of the CH_2OH and CHOH groups are likewise in the trans position. In the γ conformation, the two oxygen atoms of the CH_2OH groups are also trans with respect to the aliphatic hydrogen atom of the CHOH group. It is reported that, owing to formation of intermolecular H bonds, glycerol in the crystalline phase consists exclusively of $\alpha\alpha$ conformers,[23] with each molecule involved in six intermolecular H-bonds. Furthermore, molecular dynamics studies indicated that intramolecular H-bonds in glycerol give rise to the formation of five-

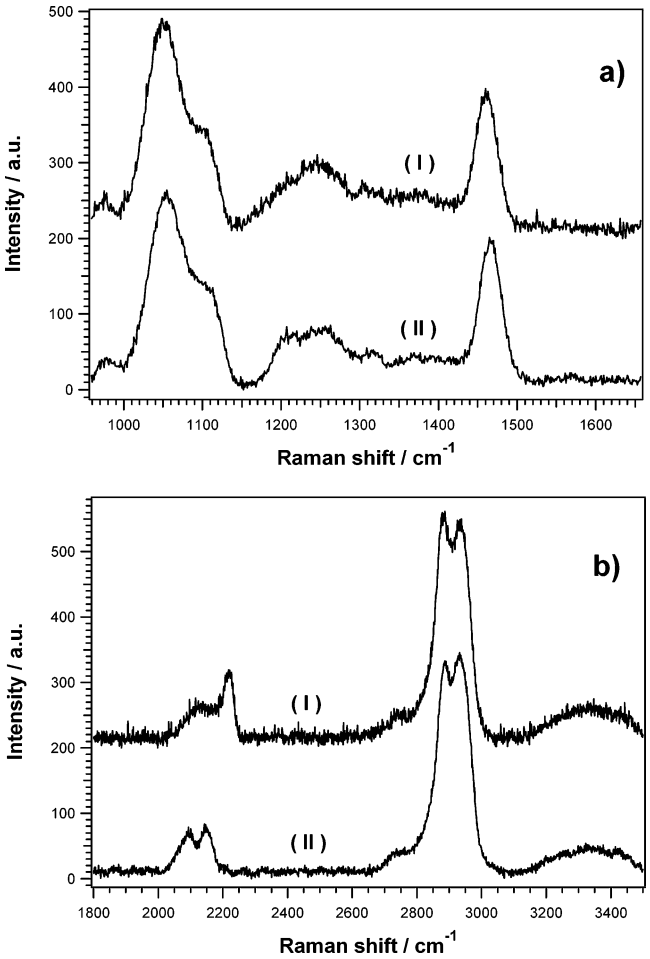

Figure 4. Raman spectra of $[Fe_xPd_y(CN)_zCl_t(C_3H_8O_3)Li_e]$ (**I**) and $Fe_xSn_y(CH_3)_{2y}(CN)_zCl_t(C_3H_8O_3)Li_e]$ (**II**) HGEs collected with parallel polarized incident light: (a) 950−1650 cm^{-1} region and (b) 1800−3500-cm^{-1} region. The laser excitation line was at 514.5 nm.

and six-atom rings closed by H-bonds.[26] Five-member rings occur in the αα and αγ conformers and six-member rings are predicted for the less abundant and stable γγ conformers.[23,26]

The Raman spectra of HGEs **I** and **II** are shown in Figure 4. The correlative assignment of the glycerol Raman bands is summarized in Table 2 and confirms the FT-IR results. Taken together, the MIR FT-IR and Raman investigations allow us to conclude that (a) the interactions experienced by glycerol units in the bulk materials are only slightly different from those registered in pristine liquid glycerol[23] and (b) glycerol is constituted of three types of conformers (αα, αγ, and γγ). With respect to the most stable γγ conformer, whose energy was assumed to be 0, the energies of the most stable αγ and γγ conformers[23] differ by ca. 5.2 and 10.1 kJ mol^{-1}, respectively.

The far-IR spectra of the two HGEs are depicted in Figure 3b, and their assignments are provided in Table 2. A careful inspection of the far-IR spectra shows that they are the result of the addition of glycerol and metal−ligand vibrational modes. In particular, the stretching bands of ν(Fe−CN), ν^a(Pd−N), ν^s(Pd−N), ν(Pd−O), ν(Li−O), δ(C−Fe−C), and ν^a(Pd−Cl) are evident in the spectrum of HGE **I**, while the spectrum of **II** reveals the vibrational modes of ν(Fe−CN), ν(Sn−O), ν(Sn−C), ν(Li−O), ν(Sn−N), and ν(Sn−Cl) stretching. These results confirm the above-reported suggestion that the two HGEs are formed owing to the substitution of chloride ligands in $[PdCl_4^{2-}]$ (**I**) or $(CH_3)_2SnCl_2$ (**II**) by nitrogen cyanometalate groups and oxygen atoms of glycerol hydroxyl groups. Semiquantitative information regarding the concentration of bridging and terminal cyanide groups in the HGE materials was obtained by Gaussian spectral decomposition of the MIR spectra[3−8] in the 1900−2250-cm^{-1} range (Figure 5).

Table 3 reports the peak position, band area (A_i), full width at half-maximum ($fwhm_i$), and experimental and theoretical percentage of different types of CN groups present in **I** and **II**. Spectral decomposition of the cyanide region of HGE **I** revealed the presence of six bands (Figure 5 (**I**)).

The vibrational modes peaking at 2025, 2063, and 2186 cm^{-1} were assigned to terminal CN groups of $[Fe(CN)_6]^{3-}$ moieties $[\nu(-CN)_t]$, while the bands at 2158, 2185, and 2218 cm^{-1} were attributed to the CN stretchings $[\nu(-CN)_b]$ of Fe−CN−Pd bridges. For HGE **II**, four CN bands were measured. The two peaks at 2038 and 2073 cm^{-1} were assigned to the terminal stretching vibrations of CN groups $[\nu(CN)_t]$, and the bands at 2103 and 2144 cm^{-1} were assigned to the vibrations of bridging cyanides $[\nu(CN)_b]$. The percentage of each type of structurally different CN with respect to the total number of CN groups was determined by the formula $R_i^{CN} = A_i^{CN} \times 100/\sum A_i^{CN}$ (Table 3).

Furthermore, the band areas permit us to calculate the fractional amount of bridging (R_b^{CN}) and terminal (R_t^{CN}) CN groups. For HGE **I**, the values of R_b^{CN} and R_t^{CN} were 0.19 and 0.81, respectively; for HGE **II** they were 0.37 and 0.63, respectively (Table 3). These observations indicate that in HGE **I**, among 6 CN groups, one is probably of the bridging type and five are terminal cyanides, while in HGE **II**, among 6 CN groups, two are bridging and four are terminal cyanides.

To obtain more detailed information regarding the structures of these materials, the data shown in Table 1 were used to calculate the following ratios for HGE **I**: $f_I^{\mathbf{M}} = (n_{\mathbf{I}}^{Pd} + n_{\mathbf{I}}^{Fe}/N^{\mathbf{I}}) = 0.0197 \cong 5/254$, $f_{gly}^{\mathbf{I}} = n_{\mathbf{I}}^{gly}/N^{\mathbf{I}} = 0.9803 \cong 249/254$, $f_{Pd}^{\mathbf{I}} = n_{\mathbf{I}}^{Pd}/N_M^{\mathbf{I}} = 0.60 \cong 3/5$, and $f_{Fe}^{\mathbf{I}} = n_{\mathbf{I}}^{Fe}/N_M^{\mathbf{I}} = 0.4 \cong 2/3$, where $N^{\mathbf{I}} = n_{\mathbf{I}}^{Pd} + n_{\mathbf{I}}^{Fe} + n_{\mathbf{I}}^{gly}$ and $N_M^{\mathbf{I}} = n_{\mathbf{I}}^{Pd} + n_{\mathbf{I}}^{Fe}$, with $n_{\mathbf{I}}^{Pd}$, $n_{\mathbf{I}}^{Fe}$, and $n_{\mathbf{I}}^{gly}$ being the moles of Pd, Fe, and glycerol, respectively, in 100 g of HGE **I**. On the basis of $f_M^{\mathbf{I}}$ and $f_{gly}^{\mathbf{I}}$ we can conclude that 254 mol of material will contain 5 mol of metals, i.e., 2 Fe and 3 Pd atoms. Taking into consideration the MIR and far-IR results reported above for **I** we can hypothesize the structure for HGE **I** reported in Scheme 2. Similar analysis of HGE **II** yielded the following: $f_M^{\mathbf{II}} = (n_{\mathbf{II}}^{Sn} + n_{\mathbf{II}}^{Fe}/N^{\mathbf{II}}) = 0.02422 \cong 7/289$, $f_{gly}^{\mathbf{II}} = n_{\mathbf{II}}^{gly}/N^{\mathbf{II}} = 0.9758 \cong 282/289$, $f_{Sn}^{\mathbf{II}} = n_{\mathbf{II}}^{Sn}/N_M^{\mathbf{II}} = 0.71 \cong 5/7$, and $f_{Fe}^{\mathbf{II}} = n_{\mathbf{II}}^{Fe}/N_M^{\mathbf{II}} = 0.29 \cong 2/7$, where $N^{\mathbf{II}} = n_{\mathbf{II}}^{Sn} + n_{\mathbf{II}}^{Fe} + n_{\mathbf{II}}^{gly}$ and $N_M^{\mathbf{II}} = n_{\mathbf{II}}^{Sn} + n_{\mathbf{II}}^{Fe}$ with $n_{\mathbf{II}}^{Sn}$, $n_{\mathbf{II}}^{Fe}$, and $n_{\mathbf{II}}^{gly}$ being the moles of Sn, Fe, and glycerol, respectively, in 100 g of the HGE **II**. These results combined with the information obtained from the study of cyanide groups and far-IR investigations allowed us to hypothesize the structural model for HGE **II** reported in Scheme 3.

In summary, it can be concluded that the proposed HGE materials consist of inorganic−organic networks in which structural units of clusters of Fe and Pd (or Sn) are bonded together through glycerol bridges, and that the cavities generated from the hybrid backbones are flooded with $[CH_2OHCHOHCH_2OH]/(LiCl)_x$ liquid electrolytes formed in situ (where x is 0.05 and 0.02 respectively for HGEs **I** and **II**). In addition, the bulk cavities in both **I** and **II** HGEs contain glycerol molecules, predominantly as αα, αγ, and γγ conformers, which are involved in lithium cation coordination and in glycerol−glycerol and glycerol−inorganic component hydrogen bonding interactions.

Further information in agreement with the proposed structural models was derived from the analysis of UV−visible spectra

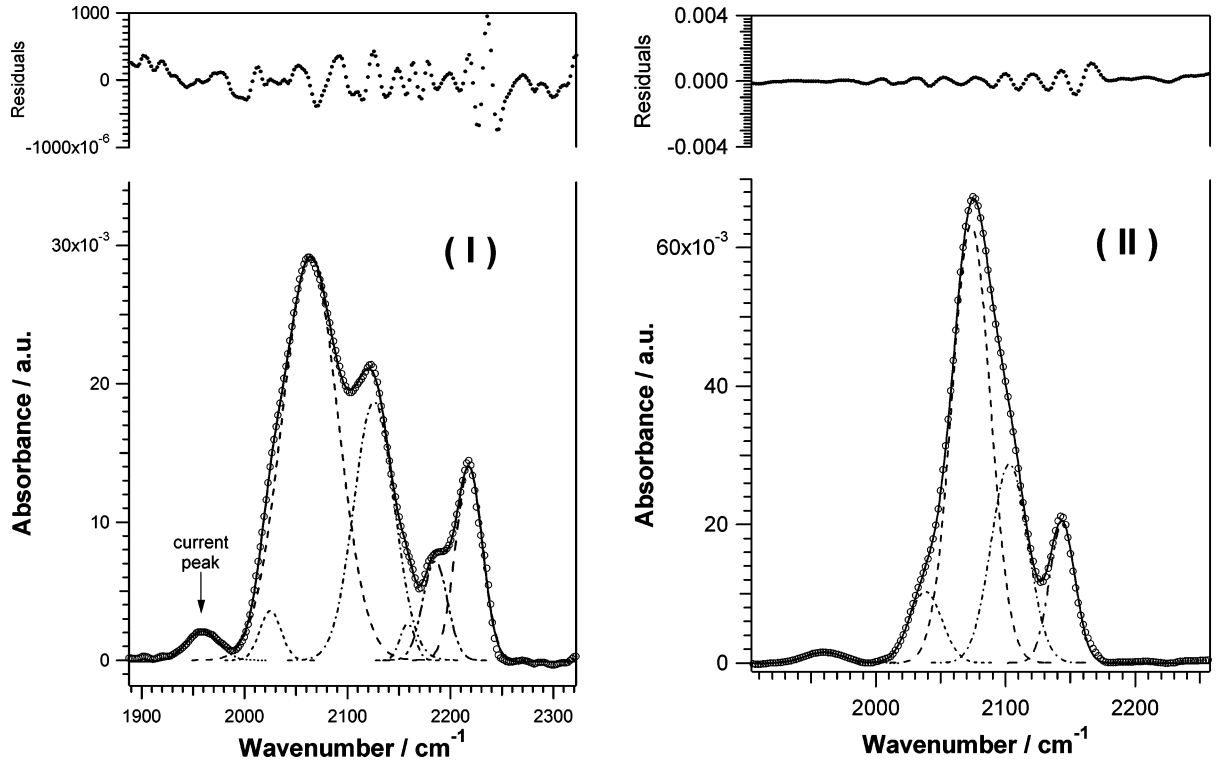

Figure 5. Decomposition by Gaussian functions of the MIR FT-IR spectral range from 1900 to 2500 cm^{-1} of $[Fe_xPd_y(CN)_zCl_t(C_3H_8O_3)Li_e]$ (**I**) and $[Fe_xSn_y(CH_3)_{2y}(CN)_zCl_t(C_3H_8O_3)Li_e]$ (**II**) HGEs.

TABLE 3: Band Parameters of the ν(CN) FT-IR Vibrational Modes for Complexes I and II

compd	band	ν_i (cm^{-1})	A_i^{CN} [a]	$fwhm_i$	R_i^{CN} (%)[b]	R_i^{CN} [c,d]	R_{teo}^{CN}
I	$\nu(-CN)_b$	2218	0.45 ± 0.01	30.4 ± 0.5	12.19	$R_b^{CN} = 0.19$	≈1/6
		2185	0.21 ± 0.01	28.1 ± 1.7	5.69		
		2158	0.05 ± 0.01	17.2 ± 2.0	1.35		
	$\nu(-CN)_t$	2126	0.92 ± 0.02	46.4 ± 0.9	24.93	$R_t^{CN} = 0.81$	≈5/6
		2063	1.97 ± 0.03	63.6 ± 1.0	53.39		
		2025	0.09 ± 0.01	24.3 ± 2.0	2.44		
II	$\nu(-CN)_b$	2144	0.50 ± 0.02	23.3 ± 0.7	12.08	$R_b^{CN} = 0.37$	≈2/6
		2103	1.02 ± 0.7	33.4 ± 4	24.63		
	$\nu(-CN)_t$	2073	2.3 ± 0.3	34.7 ± 3	55.56	$R_t^{CN} = 0.63$	≈4/6
		2038	0.32 ± 0.07	29.6 ± 3	7.73		

[a] A_i and $fwhm_i$ are the band area and the full width at half-maximum of the peak centered at ν_i, respectively. [b] R_i^{CN} (%) = $(A_i^{CN} \times 100/\Sigma A_i^{CN})$. [c] $R_b^{CN} = (\Sigma A_i^b/\Sigma A_i^{CN})$; A_i^b is the band area of bridging CN groups. [d] $R_t^{CN} = (\Sigma A_i^t/\Sigma A_i^{CN})$; A_i^t is the band area of terminal CN groups.

presented in Figure 6. In the case of HGE **I** (Figure 6a), the interpretation of the spectral data is quite straightforward if we consider the existence of two regions. The first region is dominated by spectral features of Fe(III) and includes[27] the bands peaking at 27 222 and 35 341 cm^{-1}, assigned to the Ligand to Metal Charge Transfer (LMCT) bands, σ (CN) $t_{1u} \rightarrow t_{2g}$ (Fe) and π (CN) $t_{2u} \rightarrow t_{2g}$ (Fe), respectively.[27] The second region, in which the contribution of Pd moieties prevails,[28] contains peaks at 45 109, 47 880, and 50 547 cm^{-1}. These peaks were assigned[27,28] to LMCT (Cl) $\pi_h \rightarrow xy$ (Pd) and (Cl) $\sigma \rightarrow xy$ (Pd) and Metal to Ligand Charge Transfer (MLCT) (Fe) $t_{2g} \rightarrow t_{2u}$ π^* (CN), respectively. These results are in agreement with previous findings[8] made for the Z-IOPE $[Fe_xPd_y(CN)_zCl_t(C_{2n}H_{4n+2}O_{n+1})Li_l]$.

In HGE **II** (Figure 6b), all electronic peaks are determined by the presence of Fe(III) units, since Sn moieties do not contribute to the UV−visible spectrum.[27] These peaks, at 22 821, 30 934, 39 695, 41 663, and 44 431 cm^{-1}, were assigned[27] to LMCT bands σ (CN) $t_{1u} \rightarrow t_{2g}$ (Fe), π (CN) $t_{2u} \rightarrow t_{2g}$ (Fe), and π (CN) $t_{1u} \rightarrow t_{2g}$ (Fe) and MLCT bands (Fe) $t_{2g} \rightarrow t_{1u}$ π^* (CN) and (Fe) $t_{2g} \rightarrow t_{2u}$ π^* (CN), respectively. The band at 26 022 cm^{-1} was attributed to a d−d transition of Fe, due to the lowering of the symmetry of bridging ferricyanide.[27]

The observed electronic bands indicate that Fe atoms in the cyanometalate units of both HGE systems are mostly present in oxidation state III, although the presence of traces of Fe(II) below the detection limit of the technique cannot be excluded. As expected, the electronic band shift of identical transition is determined by the coordination differences in the samples.[27] Beyond 50 000 cm^{-1}, the ultraviolet cutoff of glycerol is detected.

3.4. ^{1}H and ^{7}Li NMR Studies. Further insight about the structural characteristics of the samples, with some information regarding their dynamic behavior, was obtained by means of NMR spectroscopy. Both ^{1}H and ^{7}Li line width data for samples **I** and **II** are shown in Figure 7 a). Sample **I** shows a slight line width decrease with increasing temperature, indicating a modest thermally activated mobility for both nuclei. A similar behavior was observed for protons in sample **II**. This latter compound, however, displayed the highest mobility, as is evident from the smaller line width values. On the other hand, lithium line width remained unaffected over the entire temperature range.

SCHEME 2: Structural Model Proposed for the $[Fe_xPd_y(CN)_zCl_v(C_3H_8O_3)Li_e]$ HGE (I)

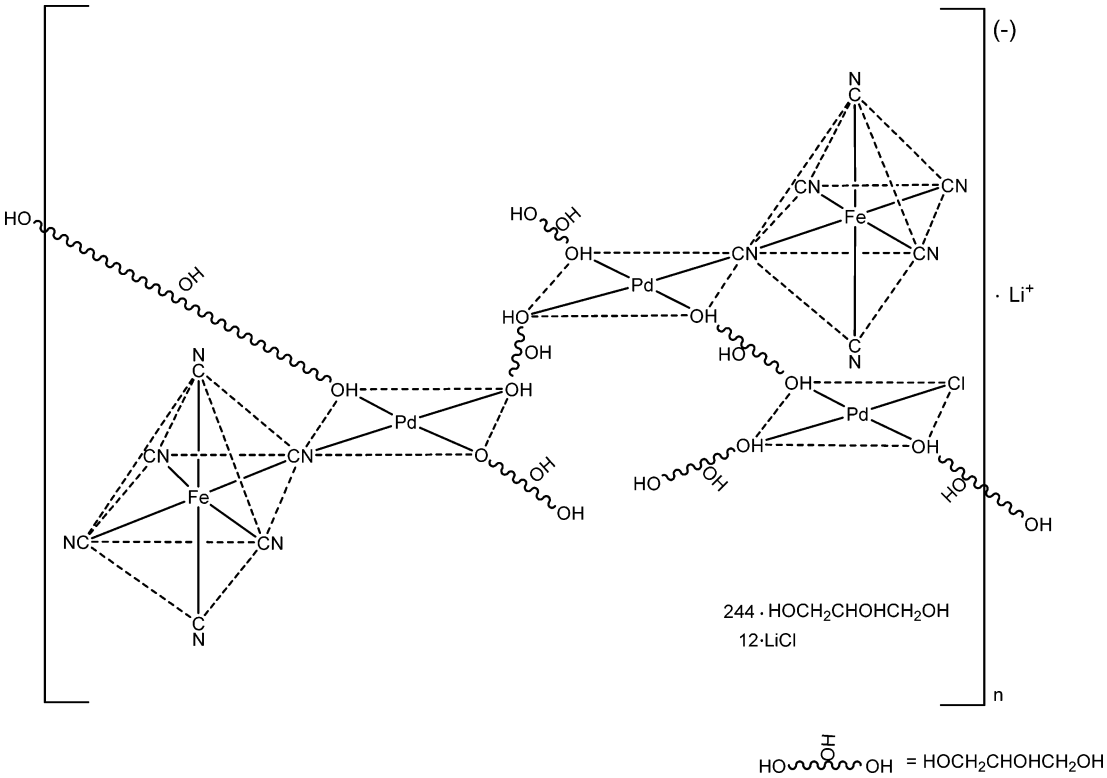

SCHEME 3: Structural Model Proposed for the $[Fe_xSn_y(CH_3)_{2y}(CN)_zCl_v(C_3H_8O_3)Li_e]$ HGE (II)

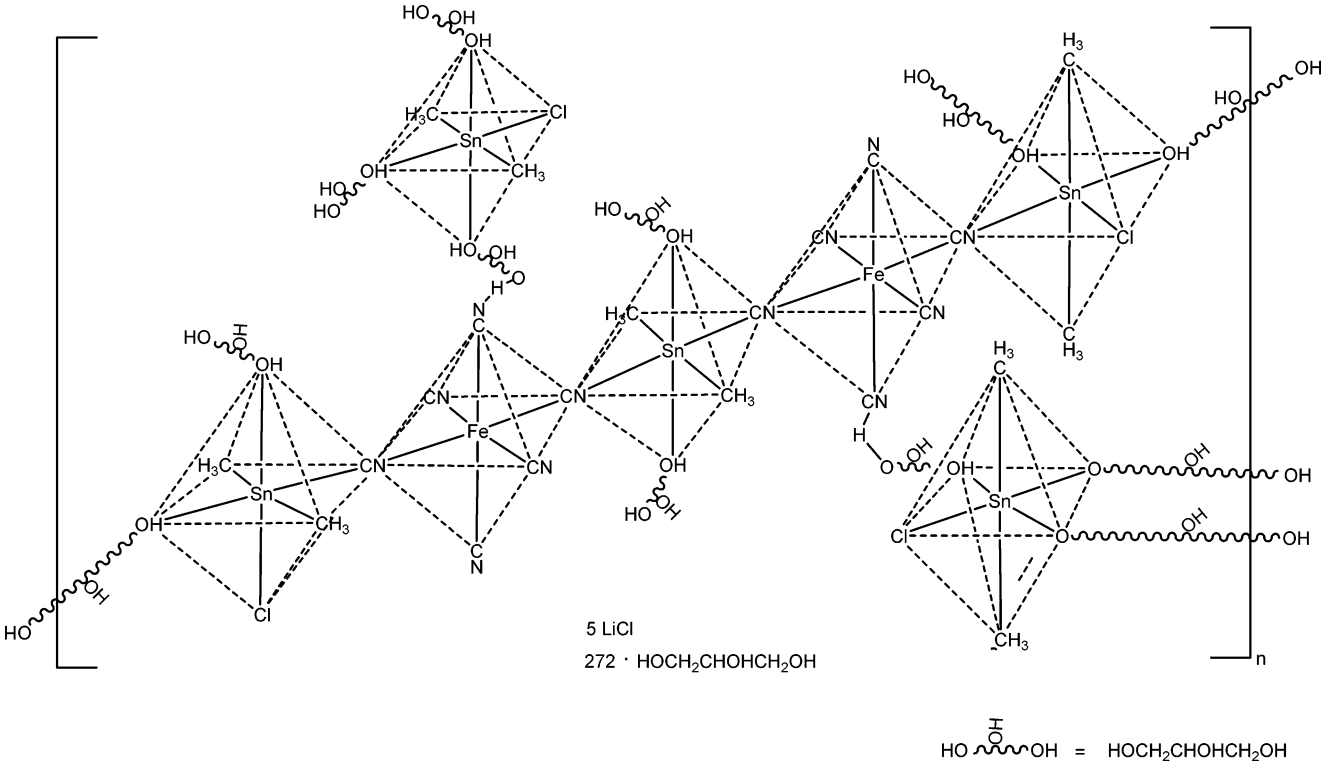

^{1}H and ^{7}Li spin−lattice relaxation (T_1) data for samples **I** and **II** are shown in Figure 7b. Proton T_1 for both samples displayed slightly decreasing profiles with increasing temperature. According to the Bloombergen−Purcell−Pound (BPP) model this indicates that we are on the rigid side of the T_1 minimum curve. This observation shows that the mobility for the protons augments as the temperature increases, in agreement with the motional narrowing shown by ^{1}H line width data. Lithium T_1 displayed little change with increasing temperature. This suggests a broad distribution of motional correlation times, implying that lithium ions experience a highly heterogeneous environment.

Measurable ^{1}H and ^{7}Li self-diffusion coefficients D are shown in Figure 7c (our measuring limit is above 5×10^{-9} cm^2/s). Proton D values were obtained for sample **II** and ranged from 10^{-8} to 10^{-7} cm^2/s. The activation energy determined by the

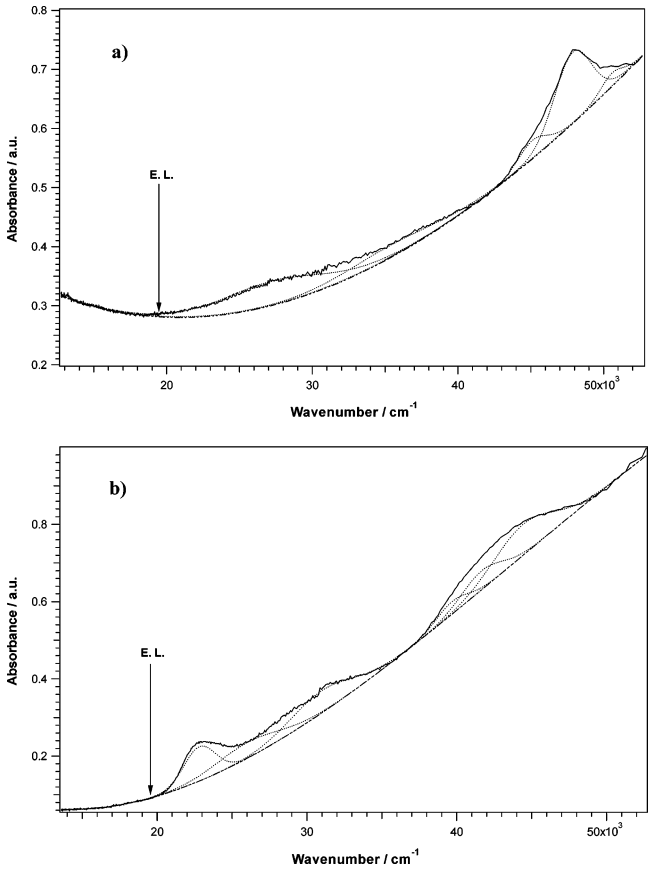

Figure 6. UV−vis spectra of (a) $[Fe_xPd_y(CN)_zCl_v(C_3H_8O_3)Li_e]$ (**I**) and (b) $Fe_xSn_y(CH_3)_{2y}(CN)_zCl_v(C_3H_8O_3)Li_e]$ (**II**). E.L. is the position of the laser excitation line (514.5 nm or 19436 cm^{-1}) used for Raman investigations. The spectral decomposition by Gaussian functions is reported.

Arrhenius equation is 9.937 ± 0.001 J/mol. This value is much lower than that found for a lithium Z-IOPE system previously studied,[9] which was ca. 20 kJ/mol. This suggest that the viscosity of sample **II** does not change much within the investigated temperature interval, at least where D is detectable. The presence of proton and lack of lithium diffusion in sample **II** suggests that the lithium ions are not subject to long-range mobility with glycerol molecules and may instead be experiencing short-range motion in proximity of the glycerol solvation clusters. This correlates with both line width and T_1 data, which indicates a very rigid lithium environment. Sample **I** on the other hand gave detectable diffusion only for lithium at 370 K. This indicates that lithium ion transport from a glycerol solvation cluster to another is thermally activated. This is supported by the fact that the proton T_1 values decrease with increasing temperature and also by line width data, which shows much greater values for protons than for lithium.

3.5. Broad Band Dielectric Spectroscopy Studies. The conductivity and dielectric response of HGEs **I** and **II** were investigated with accurate broad band dielectric spectroscopy (BDS) measurements in the −60 to +80 °C temperature range and in the $10^{-2} \leq f \leq 10^9$ Hz frequency range. Figures 8 and 9 show the $\epsilon'(f)/\epsilon_0$ and $\epsilon''(f)/\epsilon_0$ spectra for the two systems obtained at various temperatures over the entire frequency range investigated. It should be noted that three spectral features are easily detected in $\epsilon'(f)/\epsilon_0$ and $\epsilon''(f)/\epsilon_0$ profiles. At low frequencies, the first $\epsilon'(f)/\epsilon_0$ decrease corresponds to the effect of electrode polarization.[16,29,30] In the medium-frequency range, the second $\epsilon'(f)/\epsilon_0$ decrease, which in $\epsilon''(f)/\epsilon_0$ corresponds to a linear decrease with a slope of −1, is associated with dc

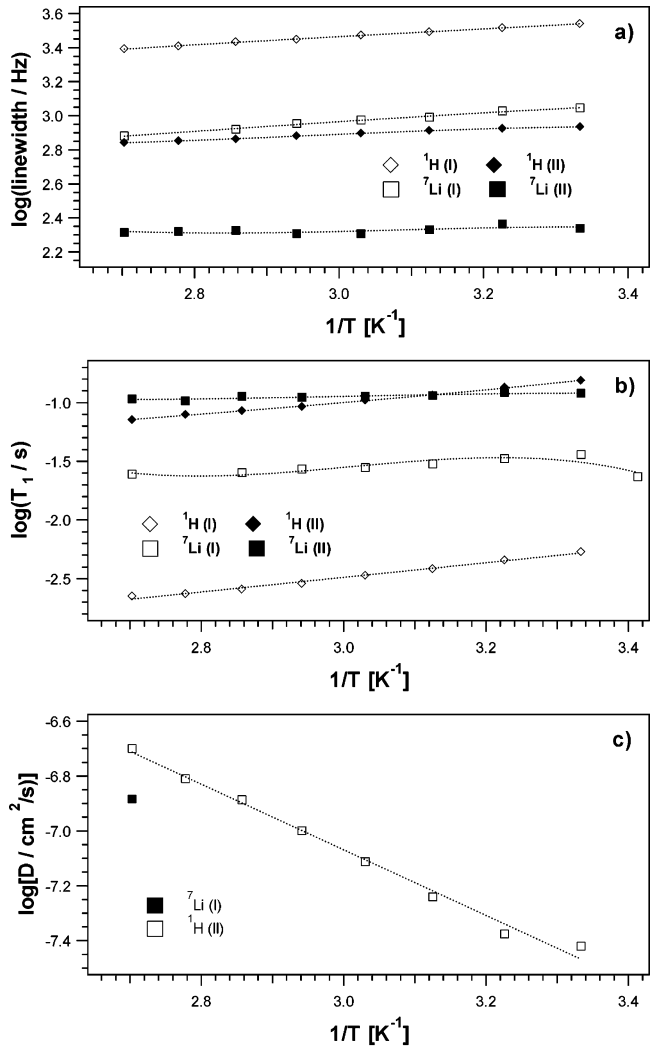

Figure 7. (a) ^1H (circles) and ^7Li (squares) NMR line width over the 300−370 K temperature range for HGE **I** (solid symbols) and HGE **II** (empty symbols). (b) ^1H (circles) and ^7Li (squares) NMR T_1's over the 300−370 K temperature range for HGE **I** (solid symbols) and HGE **II** (empty symbols). (c) ^1H (circles) and ^7Li (squares) NMR−PGSE D's over the 300−370 K temperature range for HGE **I** (solid symbols) and HGE **II** (empty symbols).

conduction.[16,29,30] The third spectral region, located at the high-frequency end, is due to dielectric relaxations.[16,29,30] This latter $\epsilon''(f)/\epsilon_0$ region exhibits relaxation peaks shifting at high frequency through the frequency window as the temperature increases.

In agreement with the literature,[11] the relaxation at high frequency in the $\epsilon''(f)/\epsilon_0$ curves is attributed to the α-relaxation peak of supercooled glycerol. This latter relaxation was interpreted in terms of a dynamic process involving the formation and decay of cages constituted by glycerol molecules bonded together through extended hydrogen-bonding interactions.[11] As suggested earlier, α-relaxation is generated by cooperative movements of glycerol molecules. Detailed analysis of the BDS spectra was carried out by using the empirical equation[16,29,30]

$$\epsilon^* = \epsilon_\infty + \sum_\infty \frac{\Delta\epsilon_k}{\{1 + (i\omega\tau_k)^{\alpha_k}\}^{\beta_k}} + \frac{\sigma_{dc}}{i\omega}\frac{(i\omega\tau_{el})^\gamma}{1 + (i\omega\tau_{el})^\gamma} \quad (1)$$

where σ_{dc} is the dc conductivity, α_k and β_k are shape parameters

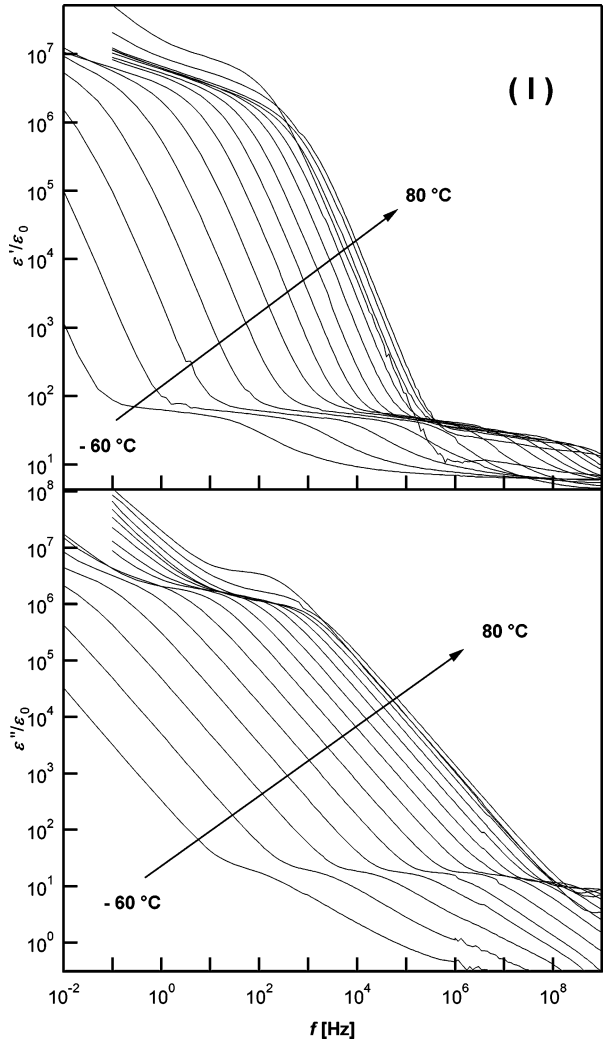

Figure 8. Real and imaginary components of dielectric spectra of HGE **I**. Measurements were performed from −60 to +80 °C in 10-deg increments.

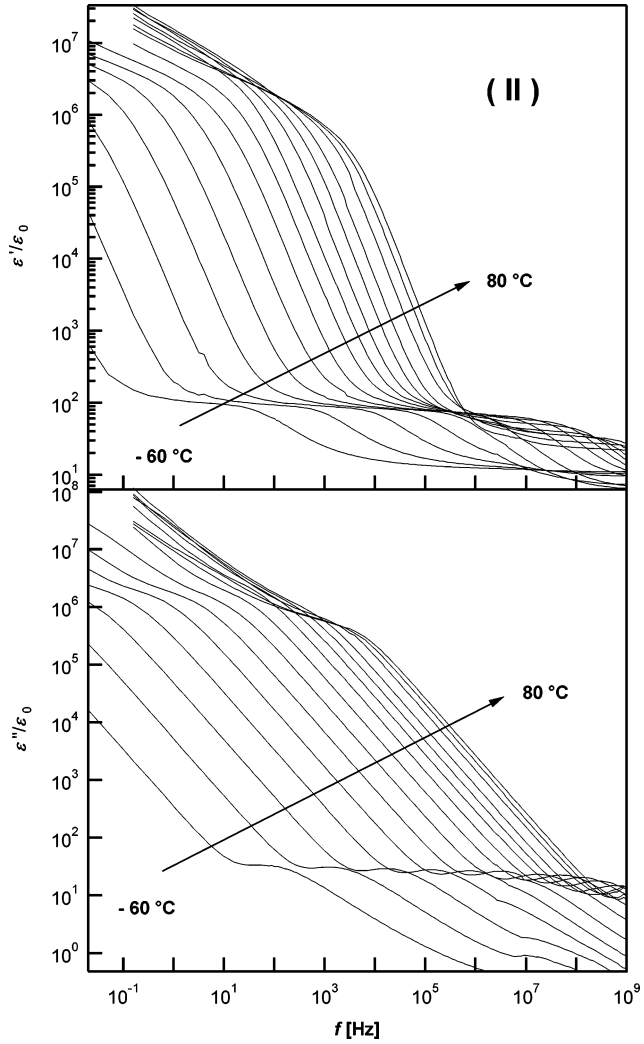

Figure 9. Real and imaginary components of the dielectric spectra of HGE **II**. Measurements were performed from −60 to +80 °C in 10-deg increments.

describing the symmetric and asymmetric broadening of the kth relaxation peak, $\tau_k = 1/(2\pi f_k)$ is the dielectric relaxation time (with f_k in Hz the frequency of peak position), $\Delta\epsilon_k$ is the relaxation strength, and τ_{el} is the relaxation time associated with the electrode polarization phenomena. Equation 1 accounts for all the spectral features observed in Figures 8 and 9. In particular, the third term in eq 1 describes the electrode polarization phenomena and dc conductivity, while the first two terms simulate the dielectric relaxations of the materials. To obtain accurate fits for the dielectric spectra, we first evaluated σ_{dc} in the medium-frequency plateau of the $\sigma'(\omega)$ profiles[31,32] and τ_{el} in the Cole−Cole representation of the conductivity data at low frequencies. Then, after fixing these latter values in eq 1, the other parameters were easily determined by fitting eq 1 to the data shown in Figures 8 and 9.

Figures 10a and 11a show fitting results at the high-frequency end of the spectra for HGEs **I** and **II**, and Figures 10b and 11b report the difference spectra obtained by subtracting the electrode polarization and σ_{dc} contribution from the dielectric spectra shown in Figures 8 and 9, respectively. Two relaxation peaks were revealed and fitted. The dominant loss peak corresponds to the α-relaxation,[11] while the weak broad peak measured at high frequencies in the low-temperature range (213−243 and 243−273 K respectively for **I** and **II**) corresponds to the slow β-relaxation mode of B glass formers.[11,14] The slow β-relaxation peak is ascribed to an internal change in the molecular conformation of glycerol.[11,14]

The charge transport mechanism processes in HGEs **I** and **II** were studied by analyzing the dependence of the parameters σ_{dc} and τ_k on temperature, shown in Figure 12, parts a and b). Results, shown in Figure 12, indicated that the dependence of σ_{dc} on temperature could be satisfactorily fitted by the well-known Vogel−Tamman−Fulcher relation (VTF).[31,32] On the other hand, as expected, the f_α data were simulated very well by the Vogel−Fulcher−Tamman−Hesse equation (VTFH),[33] and f_β values by an Arrhenius-like relation.[33] The fitting equations with the determined parameters are summarized in Table 4.

These observations reveal the following properties for the charge transport mechanism: (a) the preexponential factors for f_α and f_β relaxations are in the expected range for glycerol;[11,14,33] (b) the activation σ_{dc} energies of **I** and **II** are quite similar (i.e., ca. 32 and 37 kJ mol^{-1}, respectively) and close to the slow β-relaxation value (ca. 29 kJ mol^{-1}); and (c) for both HGEs f_α exhibits the lowest activation energy (i.e., ca. 14 kJ mol^{-1} for **I** and 13 kJ mol^{-1} for **II**). These indications suggest that the charge transfer mechanism is mainly regulated by slow β-relaxation phenomena, which, as reported above, are attributed to the internal conformational changes of glycerol molecules and probably take place when lithium coordination events occur.

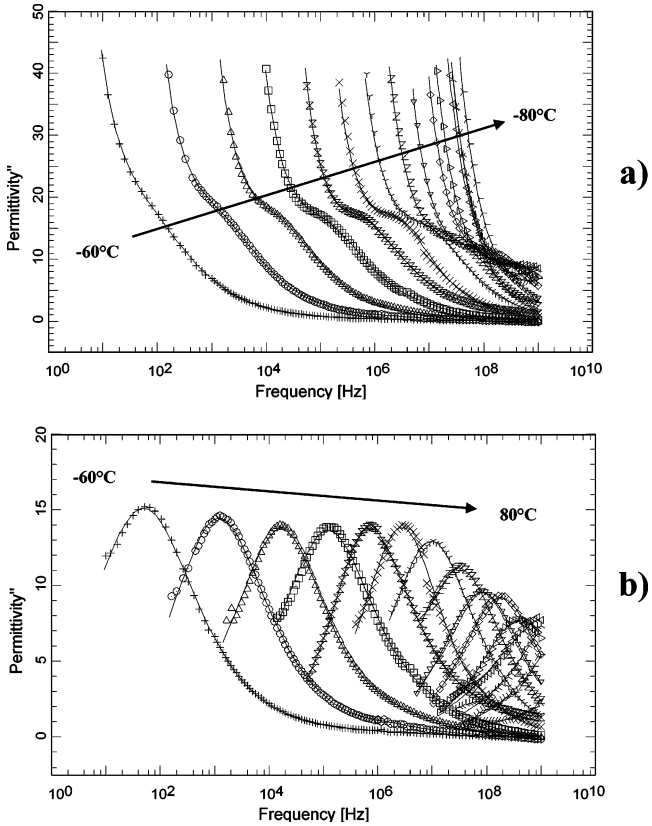

Figure 10. Imaginary component of the dielectric spectra of HGE **I**: (a) dielectric loss spectra (marks) fitted with eq 1 (solid line) and (b) difference dielectric loss spectra obtained by subtracting the spectral contribution of electrode polarization and σ_{dc} from dielectric spectra shown in part a. Measurements were performed from −60 to +80 °C in 10-deg increments.

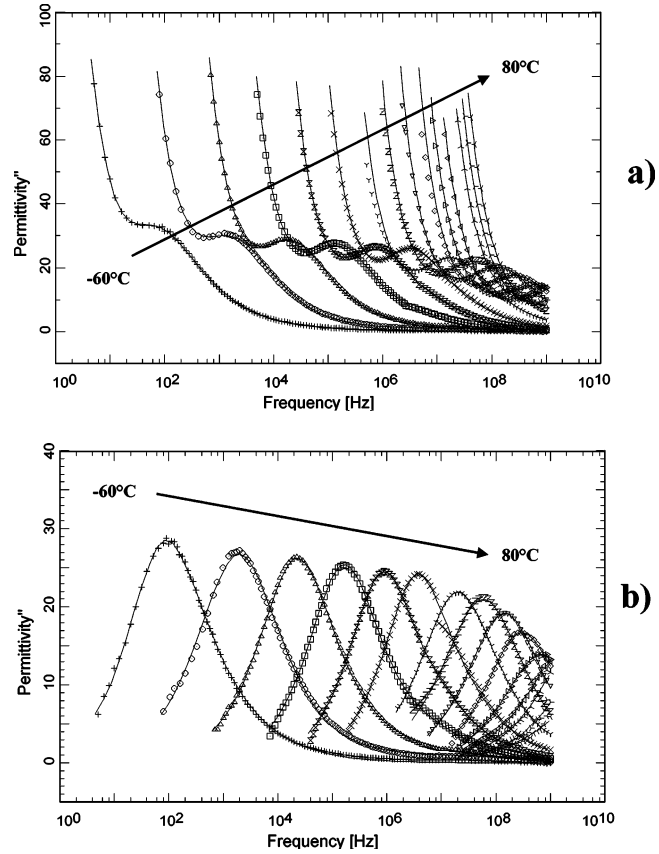

Figure 11. Imaginary component of the dielectric spectra of HGE **II**: (a) dielectric loss spectra (marks) fitted with eq 1 (solid line) and (b) difference dielectric loss spectra obtained by subtracting the spectral contribution of electrode polarization and σ_{dc} from dielectric spectra of part a. Measurements were performed from −60 to +80 °C in 10-deg increments.

In addition, the low energy barrier of α relaxation indicates that the formation and decay of glycerol cages by extended hydrogen bond interactions occur very easily, thus indicating that α relaxation is not the rate-determining phenomenon in the lithium charge-transfer mechanism. Moreover, a comparison between the activation energies of α relaxation in the two HGEs with respect to that of pristine glycerol[11] (19.20 kJ mol^{-1}) indicates that the hydrogen bond interactions are weaker in the HGE networks. These results are in agreement with the MIR FT-IR results. A further confirmation is obtained from the analysis of strength parameter *D*, which is usually used to classify glass formers:[10,11,14] $D < 10$ is typical of "fragile glass formers" and $D > 10$ characterizes "strong glass formers". Pure glycerol is a rather "strong glass former" ($D = 17.9$).[11] The *D* values calculated from the data reported in Table 4 classify HGE **I** as a modest "strong glass former" ($D = 11.5$) and **II** as a "fragile glass former" ($D = 9.7$).

Further details are obtained by analyzing the temperature dependence of the relaxation strengths $\Delta\epsilon_\alpha/\epsilon_0$ and $\Delta\epsilon_\beta/\epsilon_0$ (data not shown). The $\Delta\epsilon_\alpha/\epsilon_0$ of **II** is higher than that of **I**, indicating that polarization is higher in **II** with respect to **I**. Furthermore, as the temperature decreases $\Delta\epsilon_\alpha/\epsilon_0$ increases at $T < 40$ °C, but then diminishes at $T > 40$ °C. These findings are in accordance with the results described above and justify the classification of **I** and **II** as "strong" and "fragile" glass formers, respectively. $\Delta\epsilon_\beta/\epsilon_0$ exhibits low values and a slight temperature dependence, probably because this relaxation strength is correlated to the low lithium ion concentration present in the bulk materials. An additional confirmation of the relaxation data is provided by the analysis of shape parameters *m* and *n*,[33] where $m = \alpha_k$ and $n = \alpha_k\beta_k$, with α_k and β_k fitting parameters determined by means of eq 1. The observed *m* and *n* values (data not shown), i.e., $m \sim 1$ and $n > 0.5$ for α relaxations, are characteristic of relaxation modes in low molecular weight glass-forming liquids.[33]

Finally, we can analyze the relationship between the HGEs' diffusion constant (*D*), and migration step length (λ), and temperature, if we assume (a) the Stokes−Einstein equation connecting the diffusion constant to the viscosity of liquids[34]

$$D = kT/6\pi\eta a \tag{2}$$

where *k* is the Boltzman constant, *T* is the temperature, and *a* is the radius of a spherical object in a medium with viscosity η, and (b) the Einstein−Smoluchowski equation[30]

$$D = \lambda^2/6\tau \tag{3}$$

which describes the motion of a particle by a random walk scheme with length λ and step time τ, in the approximation that $\lambda = a$, eqs 2 and 3 yield

$$\lambda = (6\tau D)^{1/2} \text{ and } D^{3/2} = \frac{kT}{6^{3/2}\pi\tau^{1/2}\eta} \tag{4}$$

Given that HGEs **I** and **II** are constituted primarily of glycerol, and assuming that η in pristine glycerol is similar to that of glycerol embedded in **I** and **II**, the use of eq 4, together with α peak relaxation times (Figure 12) and η values reported in the literature,[35,36] permits us to determine the dependence of **D** and λ on temperature (Figure 13).

TABLE 4: Selected Parameters Determined by Fitting VTF, VTFH, and Arrhenius Equations to the Dependence of σ_{dc}, f_α, and f_β on Temperature

compd	parameter	$\sigma_{dc}(T) = A_\sigma(T^{-1/2})e^{-E_a/[R(T-T_0)]}$	$f_\alpha(T) = f_{\alpha\infty}e^{-E_\alpha/[R(T-T_0)]}$	$f_\beta(T) = f_{\beta\infty}e^{-E_\beta/RT}$
I	activation energy (kJ mol^{-1})	32.9 ± 2.4	14.2 ± 2.0	29.88 ± 0.51
	preexponential[a] factor	111 ± 13	(1.0 ± 0.2) × 10^{13}	(1.0186 ± 0.009) × 10^{13}
	T_0 (K)	143.8 ± 3.9	148.8 ± 6.7	
II	activation energy (kJ mol^{-1})	36.7 ± 1.8	12.6 ± 2.7	29.09 ± 0.31
	preexponential[a] factor	255 ± 18	(1.0 ± 0.1) × 10^{13}	(1.0046 ±0.0049) × 10^{13}
	T_0 (K)	137.7 ± 2.9	155.9 ± 9.8	

[a] The units for A_σ are S·cm^{-1}; the units for $f_{\alpha\infty}$ and $f_{\beta\infty}$ are Hz.

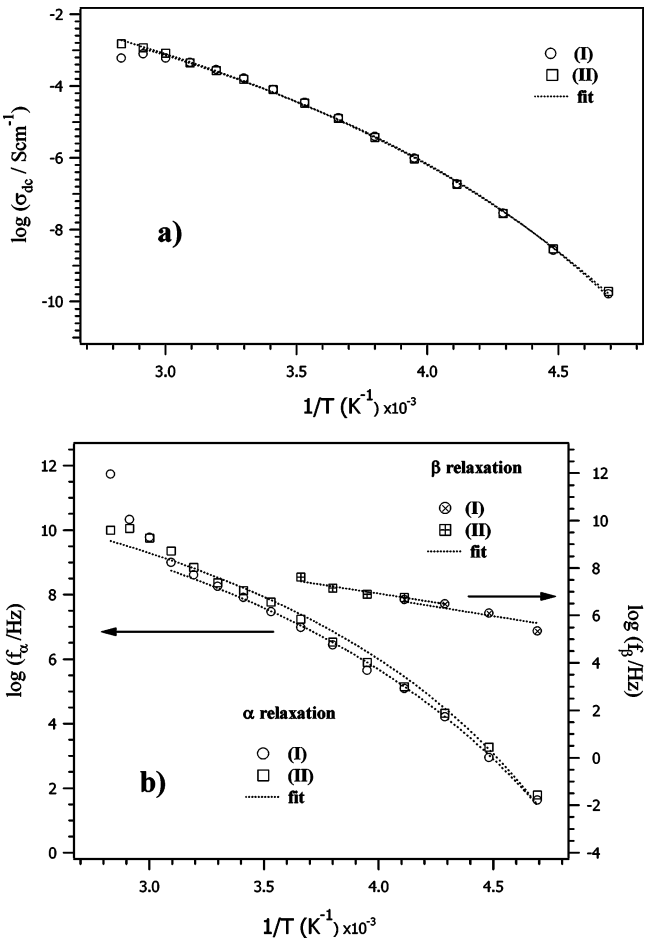

Figure 12. Dependence of σ_{dc} (a) and f_α and f_β (b) on the reciprocal of temperature in HGEs **I** and **II**.

Results show that the HGE values at temperatures higher than 290 K are in agreement with those determined by NMR measurements, and that at temperatures lower than 320 K, the formation and decay of glycerol cages take place at local short-range distances regulated by cooperative formation and rupture of hydrogen bonds. Furthermore, at temperatures lower than 290 K, λ increases with decreasing temperature, probably owing to the preferential formation of intermolecular hydrogen bonds.

On the other hand, at temperatures higher than 290 K, λ decreases as temperature rises, indicating that intramolecular hydrogen bond breakage and formation are preferred. These results indicate that at temperatures higher than 290 K, the most stable conformers are those characterized by a high number of intramolecular hydrogen bonds such as $\gamma\gamma$ (in this case the diffusion of glycerol cages is high), while at low temperatures the conformers with a high number of intermolecular hydrogen bonds are preferred (a low glycerol cage diffusion is expected in this case).

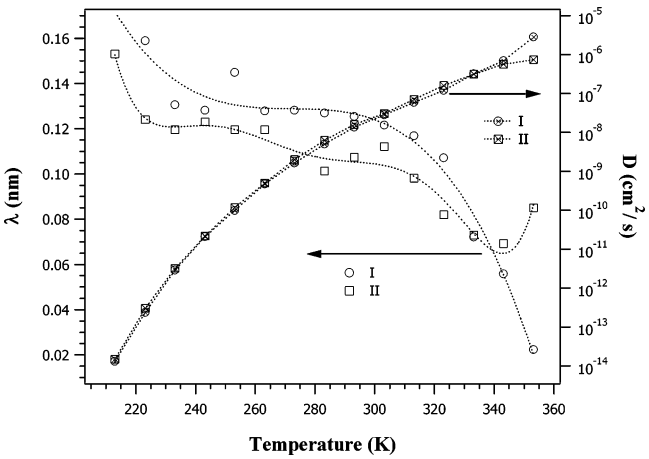

Figure 13. Temperature dependence of migration step length λ and diffusion coefficient D in HGE **I** and **II**.

In conclusion, the lithium conductivity in HGE probably occurs through a mechanism totally different from that observed in common polymer electrolytes based on polyethers.[31,32] In these latter systems, it was demonstrated that lithium migration in bulk materials takes place owing to hopping of lithium ions mediated by segmental motion of polyether chains. The results of the present study prompt us to hypothesize that lithium charge migration in the bulk material of HGEs takes place in the glycerol solvation layer of the hybrid inorganic−organic backbone, where high concentrations of $\alpha\alpha$ and $\alpha\gamma$ glycerol conformers are expected. The strong intermolecular hydrogen bond interactions in the glycerol solvation layer facilitate (a) the conformational changes of glycerol molecules forming lithium cation coordination cages and (b) the migration of lithium between neighboring glycerol cages via an ion exchange mechanism, which can be expressed as $GC_1Li^+ + GC_2 \leftrightarrow GC_1 + GC_2Li^+$, where GC is the glycerol hydrogen bonding cage.

Finally, the conductivities of 5.0 × 10^{-5} and 8.5 × 10^{-5} S·cm^{-1} measured at 25 °C for HGE **I** and **II**, respectively, classify these materials as good ionic conductors.

4. Conclusions

This paper reports the preparation, structural characterization, and extended study of ion conduction dynamics in two new hybrid inorganic−organic gel materials based on either Li_2PdCl_4 or $(CH_3)_2SnCl_2$ plus $Li_3Fe(CN)_6$ and glycerol as precursors. Two HGE materials with the formulas $[Fe_{0.008}Pd_{0012}(CN)_{0.048}Cl_v(C_3H_8O_3)Li_{0.051}]$ (**I**) and $[Fe_{0.007}Sn_{0.018}(CH_3)_{0.036}(CN)_{0.049}Cl_v(C_3H_8O_3)Li_{0.019}]$ (**II**) were obtained through an almost instantaneous sol → gel reaction. HGEs **I** and **II** are thermally stable up to ∼115 and ∼125 °C, respectively. DSC measurements revealed that HGEs **I** and **II** have T_g values of −74 and −76 °C, respectively, with no other thermal transition registered up to sample decomposition temperatures. SEM investigations with XRD-EDS microanalyses showed that the two HGEs exhibit

homogeneous chemical composition but different morphologies. The morphology of HGE **I** is similar to that of a compact soft granular paste, while HGE **II** is a completely smooth gummy paste with a slightly wrinkled surface appearance. FT-IR, Raman, and UV−vis studies allowed us to conclude that these materials consist of mixed inorganic−organic networks containing cavities flooded with glycerol glass-former lithium electrolyte materials. The hybrid inorganic−organic networks in HGE **I** are constituted of Pd atoms bound to Fe by CN bridges, and Pd atoms linked together by glycerol bridges. Likewise the networks in HGE **II** are composed of Sn atoms bound to Fe through CN bridges and Sn atoms linked together by glycerol. FT-IR and Raman studies revealed that the glycerol molecules in lithium electrolyte glass formers flooding the HGEs' bulk cavities are predominantly a mixture of $\alpha\alpha$, $\alpha\gamma$, and $\gamma\gamma$ conformers.

Variable-temperature ^{1}H and ^{7}Li NMR line width spin−lattice relaxation and pulsed field gradient diffusion measurements suggested that lithium ion transport in the HGEs differs from that in common polyether based polymer electrolytes. Indeed, charge transport in HGEs occurs via short-range motions within glycerol solvation clusters.

Broad band dielectric spectroscopy investigations carried out in the 10 mHz to 1 GHz range and from −60 to +80 °C were in accordance with NMR results and revealed that the conductivity of the two HGEs is modulated by the α and slow β mode relaxations of glycerol glass-forming molecules. Furthermore, accurate analyses of the temperature dependence of the mode relaxation parameters and of σ_{dc} values indicated that ion diffusion in electrolytes flooding the HGEs' cavities takes place over distances on the order of the magnitude of glycerol intermolecular hydrogen bond lengths. These results permit us to conclude that the two HGEs probably conduct ionically through a charge migration mechanism, which involves short-range exchange of lithium ions between glycerol coordination cages. The lithium coordination cages are generated owing to intermolecular hydrogen bonds between glycerol molecules forming the solvation layer of the hybrid inorganic−organic network backbone.

Finally, HGE **I** and **II** exhibit room temperature conductivities $\cong 5.0 \times 10^{-5}$ and 8.5×10^{-5} S·cm^{-1}, respectively, thus classifying them as good lithium electrolyte materials.

References and Notes

(1) Gray, F. M. *Polymer Electrolytes*; RSC Materials Monographs; Royal Society of Chemistry: Cambridge, UK, 1997.

(2) Tarascon, J. M.; Armand, M. *Nature* **2001**, *414*, 359.

(3) Di Noto, V. *J. Mater. Res.* **1997**, *12*, 3393.

(4) Di Noto, V. *J. Phys. Chem. B* **2000**, *104*, 10116.

(5) Di Noto, V.; Barreca, D.; Furlan, C.; Armelao, L. *Polym. Adv. Technol.* **2000**, *11*, 108.

(6) Di Noto, V.; Fauri, M.; Vittadello, M.; Lavina, S.; Biscazzo, S. *Electrochim. Acta* **2001**, *46*, 1587.

(7) Di Noto, V.; Fauri, M.; Vittadello, M.; Lavina, S.; Biscazzo, S. *Macromol. Chem. Phys.* **2002**, *203*, 354.

(8) Di Noto, V.; Vittadello, M.; Lavina, S.; Biscazzo, S.; Fauri, M. *Electrochim. Acta* **2003**, *48*, 2047.

(9) Vittadello, M.; Suarez, S.; Chung, S. M.; Fujimoto, K.; Di Noto, V.; Greenbaum, S. G.; Furukawa, T. *Electrochim. Acta* **2003**, *48*, 2227.

(10) Angell, C. A. *J. Res. Natl. Inst. Stand. Technol.* **1997**, *102*, 171.

(11) Lunkenheimer, P.; Schneiner, U.; Brand, R.; Loidl, A. *Contemp. Phys.* **2000**, *41*, 15.

(12) Ito, K.; Moynihan, C. T.; Angell, C. A. *Nature* **1999**, *398*, 492.

(13) Martinez, L. M.; Angell, C. A. *Nature* **2001**, *410*, 663.

(14) Kudlik, A.; Benkhof, S.; Blochowicz, T.; Tschirwitz, C.; Rössler, E. *J. Mol. Struct.* **1999**, *479*, 201.

(15) Forsyth, M.; MacFarlane, D. R.; Hill, A. J. *Electrochim. Acta* **2000**, *45*, 1243.

(16) Furukawa, T.; Imura, M.; Yuruzume, H. *Jpn. J. Appl. Phys.* **1997**, *36*, 1119.

(17) Cotton, F. A.; Wilkinson, G. *Advanced Inorganic Chemistry*, 5th ed,; J. Wiley and Sons; New York, 1998.

(18) Greenwood, N. N.; Earnshaw, A. *Chemistry of the Elements*, 3rd ed.; Butterwarth-Heinemann Ltd: Oxford, UK, 1995; p 461.

(19) Vien, D. L.; Coltup, N. B.; Fateley, W. G.; Grasselli, J. G. *The Handbook of Infrared and Raman Characteristic Frequencies of Organic Molecules*; Academic Press: Boston, MA, 1991.

(20) Di Noto, V.; Longo, D.; Münchow, V. *J. Phys. Chem.* **1999**, *103*, 2636.

(21) Nakamoto, K. *Infrared and Raman Spectra of Inorganic and Coordination Compounds*, 4th ed.; John Wiley and Sons: New York, 1986; p 272.

(22) El-Sayed, M. F. A.; Sheline, R. K. *J. Inorg. Nucl. Chem.* **1958**, *6*, 187.

(23) Chelli, R.; Gervasio, F. L.; Gellini, C.; Procacci, P.; Cardini, G.; Schettino, V. *J. Phys. Chem. A* **2000**, *104*, 5351.

(24) Bermejo, F. J.; Criado, A.; de Andres, A.; Enciso, E.; Schober, H. *Phys. Rev. B* **1996**, *53*, 5259.

(25) Bastiansen, O. *Acta Chem. Scand.* **1949**, *3*, 415.

(26) Chelli, R.; Procacci, P.; Cardini, G.; Califano, S. *Phys. Chem. Chem. Phys.* **1999**, *1*, 879.

(27) Lever, A. B. P. *Inorganic Electronic Spectroscopy, Studies in Physical and Theoretical Chemistry*, 2nd ed.; Elsevier: Amsterdam, The Netherlands, 1984; p 261.

(28) Lever, A. B. P. *Inorganic Electronic Spectroscopy, Studies in Physical and Theoretical Chemistry*, 2nd ed.; Elsevier: Amsterdam, The Netherlands, 1984; p 343.

(29) Kano, K.; Takahashi, Y.; Furukawa, T. *Jpn. J. Appl. Phys.* **2001**, *40*, 3246.

(30) Furukawa, T.; Mukasa, Y.; Suzuki, T.; Kano, K. *J. Polym. Sci. B, Polym. Phys.* **2002**, *40*, 613.

(31) Di Noto, V.; Vittadello, M.; Lavina, S.; Fauri, M.; Biscazzo, S. *J. Phys. Chem. B* **2001**, *105*, 4584.

(32) Di Noto, V. *J. Phys. Chem. B* **2002**, *106*, 11139.

(33) Schönhals, A. In *Dielectric Spectroscopy of Polymeric Materials*; Runt, J. P., Fitzgerald, J. J., Eds.; American Chemical Society: Washington, DC, 1997; p 81.

(34) Atkins, P. W. *Physical Chemistry*, 2nd ed.; Oxford University Press: Oxford, UK, 1983; p 905.

(35) Carpenter, M. R.; Davies, D. B.; Matheson, A. J. *J. Chem. Phys.* **1967**, *46*, 2451.

(36) Cook, R. L.; King, H. E.; Herbst, C. A.; Herschbach, D. R. *J. Chem. Phys.* **1994**, *100*, 5178.